Frascati Physics Series Vol. 72 (2022)
7TH YOUNG RESEARCHERS' WORKSHOP 'PHYSICS CHALLENGES IN THE LHC ERA'
July 11 and 14, 2022

MULTI-STEP PHASE TRANSITIONS AND GRAVITATIONAL WAVES IN THE INERT DOUBLET MODEL

Nico Benincasa
National Institute of Chemical Physics and Biophysics, Rävala 10, Tallinn, Estonia
Luigi Delle Rose
Dipartimento di Fisica, Università della Calabria, I-87036 Arcavacata di Rende, Cosenza, Italy
Kristjan Kannike
National Institute of Chemical Physics and Biophysics, Rävala 10, Tallinn, Estonia
Luca Marzola
National Institute of Chemical Physics and Biophysics, Rävala 10, Tallinn, Estonia

Abstract

The inert doublet model is a well-motivated extension of the Standard Model that contains a dark matter candidate and modifies the dynamics of the electroweak symmetry breaking. In order to detail its phenomenology, we perform a comprehensive study of cosmic phase transitions and gravitational wave signals implied by the framework, accounting for the latest results of collider experiments. We require the neutral inert scalar to constitute, at least, a subdominant part of the observed dark matter abundance. While most of the phase transitions proceed through a single step, we identify regions of the parameter space where the electroweak vacuum is reached after multiple phase transitions. The resulting gravitational wave spectrum is generally dominated by single-step transitions and, in part of the parameter space, falls within the reach of near-future gravitational wave detectors such as LISA or BBO. We find that direct detection experiments efficiently probe the part of parameter space associated with multi-step phase transitions, which remain unconstrained only in the Higgs resonance region.

1 Introduction

Although the discovery of the Higgs boson at the LHC [16, 2] brought to completion the search for Standard Model (SM) particles, we are far from having a complete description of Nature. The cosmological observations of the last thirty years, for instance, have revealed that the SM constituents explain only a small share of the total energy budget of the Universe. In particular, the analysis of the microwave radiation background shows that baryons constitute only about 15% of all matter [3]. The remaining part is accounted for by dark matter (DM), a substance of unknown nature which finds no description in the SM. Presently, the leading direct detection experiments have not yet found clear signals of DM scattering on nucleons or electrons, resulting in upper bounds on the direct detection cross sections [4, 7, 35]. Similarly, this far collider searches have not found any presence of DM particles in the produced states [1].

This lack of signals gives encouragement to look for other avenues in the attempt to pinpoint the possible physics beyond the SM. In the present paper we revisit the phenomenology of the Inert Doublet Model (IDM) [23, 34, 10, 31], paying special attention to the reach of future gravitational-wave (GW) experiments.

With the present paper, we intend to improve on existing analyses pertaining to cosmic phase transitions (PT) within the IDM. To this purpose, we analyze the parameter space allowed by the latest collider and DM searches in the attempt to map the available phase transition patterns, as well as the GW signals they produce. Although most commonly the EW phase transitions occur in a single step ($O \to h$), we find regions of the parameter space where two-step ($O \to H \to h$ or $O \to hH \to h$) and even three-step ($O \to H \to hH \to h$) transitions are realised. We pay particular attention to two- and three-step processes that involve multiple first-order phase transitions, which have the potential to generate a clear GW signature presenting multiple peaks in the spectrum.

2 The inert doublet model

2.1 Tree-level potential

The SM Higgs doublet H_1 and the inert doublet H_2 can be decomposed as

$$H_1 = \begin{pmatrix} G^+ \\ \frac{v+h+iG^0}{\sqrt{2}} \end{pmatrix}, \qquad H_2 = \begin{pmatrix} H^+ \\ \frac{H+iA}{\sqrt{2}} \end{pmatrix}, \tag{1}$$

where h is the SM Higgs boson, $\langle h \rangle = v = 246.22$ GeV is the electroweak (EW) vacuum expection value (VEV) and G^+ and G^0 are Goldstone bosons. The inert doublet comprises a charged scalar field $H^\pm$, and two neutral scalars, H and A, with opposite CP-parities.

The tree-level potential of the model,

$$\begin{aligned} V = &-m_1^2|H_1|^2 - m_2^2|H_2|^2 + \lambda_1|H_1|^4 + \lambda_2|H_2|^4 + \lambda_3|H_1|^2|H_2|^2 + \lambda_4|H_1^\dagger H_2|^2 \\ &+ \frac{\lambda_5}{2}\left[(H_1^\dagger H_2)^2 + \text{h.c.}\right], \end{aligned} \tag{2}$$

respects a discrete $\mathbb{Z}_2$ symmetry under which H_2 is odd and all the SM fields are even. The symmetry thus ensures the stability of the lightest component of the inert doublet and forbids new Yukawa couplings between H_2 and the SM fermions, hence the epithet *inert*.

The requirement that the tree-level potential be minimised at the EW vacuum leads to the following parametrization

$$\begin{aligned} &m_1^2 = \frac{m_h^2}{2}, \qquad m_2^2 = -m_H^2 + \lambda_{345}\frac{v^2}{2}, \qquad \lambda_1 = \frac{m_h^2}{2v^2}, \qquad \lambda_3 = \lambda_{345} + 2\frac{m_{H^\pm}^2 - m_H^2}{v^2}, \\ &\lambda_4 = \frac{m_H^2 + m_A^2 - 2m_{H^\pm}^2}{v^2}, \qquad \lambda_5 = \frac{m_H^2 - m_A^2}{v^2}, \end{aligned} \tag{3}$$

given in terms of the tree-level scalar mass matrix eigenvalues m_h^2, m_H^2, m_A^2 and $m_{H^\pm}^2$ ($m_{G^0} = m_{G^\pm} = 0$ at tree-level in the EW vacuum).

The inert doublet self-coupling λ_2 does not affect DM phenomenology, but can influence the phase structure of the potential by inducing new minima at non-zero temperature. With the parametrization in eq. (3), the model is completely specified by the quantities λ_2, $\lambda_{345} \equiv \lambda_3 + \lambda_4 + \lambda_5$, and the masses m_H, $m_{H^\pm}$, m_A, which we use as input parameters in our analysis. The lightest neutral components of H_2 is a viable DM candidate. In our analysis, this role is assigned to H, in effect choosing $\lambda_5 < 0$. Equivalently,

A could be the DM candidate, related to our case through the substitutions $\lambda_{345} \leftrightarrow \tilde{\lambda}_{345} = \lambda_3 + \lambda_4 - \lambda_5$ and $m_H \leftrightarrow m_A$.[1]

For the treatment of the phase transitions in sec.4.1, we suppose that excursions in the field space occur only in the (h, H) plane, while the remaining scalar degrees of freedom are prevented from acquiring a VEV at any temperature. Therefore, the terms in the tree-level potential relevant for this analysis are

$$V_0(h, H) = -\frac{m_1^2}{2}h^2 + \frac{\lambda_1}{4}h^4 - \frac{m_2^2}{2}H^2 + \frac{\lambda_2}{4}H^4 + \frac{\lambda_{345}}{4}h^2H^2. \tag{4}$$

2.2 Coleman-Weinberg correction to the potential

The tree-level potential in eq. (2) receives important radiative contributions sourced by the one-loop n-point functions, resummed in the Coleman-Weinberg correction [19]

$$V_{\rm CW}(h, H) = \frac{1}{64\pi^2}\sum_i n_i m_i^4 \left(\ln\frac{m_i^2}{\mu^2} - C_i\right), \tag{5}$$

where $i = W, Z, t, h, H, G^0, A, G^\pm, H^\pm$ (as customary, we retain only the dominant fermion contribution given by the top quark), m_i are the eigenvalues of the field-dependent masses, μ is the renormalization scale (which we set to $\mu = v$) and C_i are constants peculiar to the renormalization scheme. The bosonic and fermionic contributions are weighted by the coefficients n_i given by $n_W = 6$, $n_Z = 3$, $n_t = -12$, $n_h = n_H = n_{G^0} = n_A = 1$ and $n_{H^\pm} = n_{G^\pm} = 2$ [22]. After using dimensional regularization with the $\overline{\rm MS}$ subtraction scheme, we have $C_i = \frac{3}{2}$ for scalars, fermions and longitudinal vector bosons, as well as $C_i = \frac{1}{2}$ for transverse vector bosons.

Following previous analyses [18, 17, 25], we compensate possible radiative shifts of the EW VEV and masses, and address the problematic Goldstone contributions with a set of counterterms specified in

$$V_{\rm CT}(h, H) = \delta m_h^2 h^2 + \delta m_H^2 H^2 + \delta\lambda_1 h^4, \tag{6}$$

2.3 Finite temperature effects

At finite temperature, thermal corrections result in a further contribution [24],

$$V_{\rm T}(h, H, T) = \frac{T^4}{2\pi}\left[\sum_i n_i^{\rm B} J_{\rm B}\left(\frac{m_i^2}{T^2}\right) + \sum_i n_i^{\rm F} J_{\rm F}\left(\frac{m_i^2}{T^2}\right)\right], \tag{7}$$

to the scalar potential. The two sums are over the boson and fermion degrees of freedom, respectively and the corresponding thermal functions [6] are

$$J_{\rm B/F}(x) = \int_0^\infty dt t^2 \ln\left(1 \mp e^{-\sqrt{t^2+x}}\right). \tag{8}$$

A consistent treatment of thermal corrections also requires the resummation of the leading self-energy daisy diagrams, which shifts the field-dependent masses

$$m_i^2(T) = m_i^2 + c_i T^2, \tag{9}$$

[1] In regard of this, notice that $\lambda_5 \to -\lambda_5$ under the substitution $m_H \leftrightarrow m_A$ and that the quartic couplings determining the DM abundance via hHH or hAA interactions are, respectively, by λ_{345} and $\tilde{\lambda}_{345}$.

by a thermal contribution quantified in the coefficients c_i [28, 36, 14]

In our analysis we use the above thermal masses when computing the quantum and the finite-temperature corrections to the tree-level potential. The full thermally-corrected effective potential is thus

$$V_{\rm eff}(h,H,T) = V_0(h,H) + V_{\rm CW}(h,H,T) + V_{\rm CT}(h,H) + V_{\rm T}(h,H,T). \tag{10}$$

3 Constraints

With the full expression of the scalar potential at hand, we briefly review the constraints applied in the forthcoming analysis.

3.1 Theoretical constraints

A first requirement is the stability of the scalar potential, which guarantees that minima appear at finite field values. For the IDM, the potential is bounded from below if the following conditions are satisfied:

$$\lambda_1 > 0, \quad \lambda_3 + 2\sqrt{\lambda_1\lambda_2} > 0, \quad \lambda_3 + \lambda_4 - |\lambda_5| + 2\sqrt{\lambda_1\lambda_2} > 0. \tag{11}$$

A charge-breaking vacuum is avoided by $\lambda_4 - |\lambda_5| < 0$, which always holds if $H^\pm$ is heavier than the DM candidate H [26].

Perturbative unitarity requires that the combinations of couplings e_i from the eigenvalues of the two-to-two scattering matrix be bounded: $|e_i| < 8\pi$. From the full 22×22 S-matrix [8], we have [13] $e_{1,2} = \lambda_3 \pm \lambda_4$, $e_{3,4} = \lambda_3 \pm \lambda_5$, $e_{5,6} = \lambda_3 + 2\lambda_4 \pm 3\lambda_5$, $e_{7,8} = -\lambda_1 - \lambda_2 \pm \sqrt{(\lambda_1-\lambda_2)^2 + \lambda_4^2}$, $e_{9,10} = -3\lambda_1 - 3\lambda_2 \pm \sqrt{9(\lambda_1-\lambda_2)^2 + (2\lambda_3+\lambda_4)^2}$, $e_{11,12} = -\lambda_1 - \lambda_2 \pm \sqrt{(\lambda_1-\lambda_2)^2 + \lambda_5^2}$. The strongest constraints are given by $|\lambda_2| < 4\pi/3$ and $|\lambda_{345}| < 4\pi$.

3.2 Experimental constraints

The decay widths of the Z and W bosons measured at LEP with high precision preclude decays of these particles into the new states. Therefore, we require that the masses of the inert doublet components satisfy [15]

$$m_H + m_{H^\pm} > m_W, \quad m_A + m_{H^\pm} > m_W, \quad m_H + m_A > m_Z, \quad 2m_{H^\pm} > m_Z. \tag{12}$$

LEP searches for new neutral final states further exclude a range of masses [33], thereby forcing

$$m_H > 80 \text{ GeV}, \quad m_A > 100 \text{ GeV} \quad \text{or} \quad \mathrm{m_A} - \mathrm{m_H} < 8 \text{ GeV}, \tag{13}$$

in addition to

$$m_{H^\pm} > 70 \text{ GeV} \tag{14}$$

due to searches for charged scalar pair production [39].

Similarly, if $m_H < m_h/2$, the Higgs boson can decay into DM with a partial width of

$$\Gamma_{h\to HH} = \frac{\lambda_{345}^2 v^2}{32\pi m_h}\sqrt{1 - \frac{4m_H^2}{m_h^2}} \tag{15}$$

which is constrained by measurements of the Higgs boson invisible width. The current values provided by the ATLAS and CMS experiments [9, 30] on the invisible branching ratio $\mathrm{BR_{inv}} = \Gamma_{h\to HH}/(\Gamma_{h\to \rm SM} + \Gamma_{h\to HH})$ are $\mathrm{BR_{inv}} < 0.23 - 0.36$. In the following, we will use the conservative limit $\mathrm{BR_{inv}} < 0.23$.

Collider analyses also provide constraints on the electroweak precision observables (EWPO), sensitive to new radiative contributions in the electroweak sector. The EWPO are usually expressed via the Peskin-Takeuchi parameters S, T and U [37, 38], determined through a joint fit of the precision observables and SM predictions. The EWPO fit within the SM alone [32] gives the results presented in tab. 1.

Parameter	Result	Correlation
S	0.06 ± 0.10	0.90 (T), -0.57 (U)
T	0.11 ± 0.12	-0.82 (U)
U	-0.02 ± 0.09	

Table 1: Peskin-Takeuchi parameters [37, 38] as determined by the electroweak precision observables [32].

The IDM contributions to the S, T and U parameters, which add to the SM result, are given by [27]

In the IDM new EWPO contributions vanish in the limit of degenerate masses, so these observables tend to discourage hierarchical mass spectra. For the purpose of constraining the IDM parameter space, we require that the total values of S, T and U remain within the 95% joint confidence level.

Finally, the properties of our DM candidate are constrained by the latest Planck measurements, which gives the corresponding relic density as $\Omega_c h^2 = 0.120 \pm 0.001$ [3]. In our analysis we impose the 3σ *upper* bound indicated by the data, although we allow for the possibility that the inert doublet yield only a subdominant DM component. For the computation of the relic abundance we rely on the `micrOMEGAs` code [12].

4 Results

In our analysis, we scan the parameter space shown in tab. 2. We then use the `CosmoTransitions` package [42] to obtain, for each point selected, the temperature-dependent phase structure of the scalar potential and to assess the nature of the corresponding phase transitions.

Parameter	Range
m_H	$[10, 1000]$ GeV
m_A	$[10, 1000]$ GeV
m_{H^+}	$[10, 1000]$ GeV
λ_2	$[0, \frac{4\pi}{3}]$
λ_{345}	$[-1.47, 4\pi]$

Table 2: The parameter ranges used in our scan. We selected only configurations with $m_H < m_A$, since H is our DM candidate. The lower bound on λ_{345} is imposed by the stability of the potential [13].

The obtained points are then selected according to the bounds discussed above.

4.1 Phase transition

The PT patterns found in our analysis are summarised in fig. 1, which schematically shows the sequences of transitions that connect the high-temperature minimum of the IDM potential, O, to the EW vacuum phase h. The red arrow indicates one-step PTs $O \to h$, which directly connect the two minima. The blue arrows characterise two-step PTs $O \to H \to h$, in which the EW vacuum is reached after a transient phase, H, where only the inert doublet neutral component acquires a VEV. Similarly, the yellow arrows denote two-step PT patterns $O \to Hh \to h$ going through a different transient phase, Hh, in which

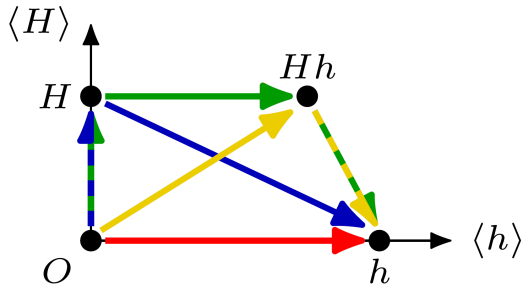

Figure 1: Schematic representation of the possible phases and PT patterns supported by the IDM scalar potential. The high-temperature minimum of the potential, where $\langle h\rangle = \langle H\rangle = 0$, is denoted with O. The phase h is characterised by $\langle h\rangle \neq 0$ and $\langle H\rangle = 0$, and includes the EW vacuum. The configuration where $\langle H\rangle \neq 0$ but $\langle h\rangle = 0$ is denoted with H, while a phase with $\langle h\rangle, \langle H\rangle \neq 0$ is indicated with Hh. The arrows show the different PT sequences identified in our analysis.

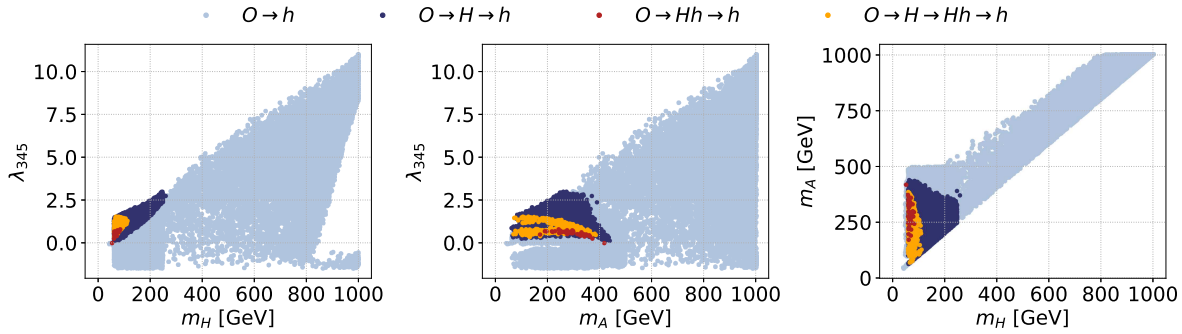

Figure 2: Projections of the IDM parameter space on the planes spanned by m_H, m_A and λ_{345}. Each panel shows the regions yielding a one-step PT $O \to h$ (light blue), a two-step PT $O \to H \to h$ (dark blue) and $O \to Hh \to h$ (red), as well as a three-step PT $O \to H \to Hh \to h$ (orange). For all these transitions, we require at least one FOPT. Points leading to DM overabundance are not shown.

both h and H acquire non-vanishing thermal VEVs. In our scan we have also identified three-step PTs $O \to H \to Hh \to h$ as indicated by the green arrows.

The sequences of PTs involving at least one first-order phase-transition (FOPT) step are presented in isolation in fig. 2. As we can see, most of the covered parameter space gives rise to one-step $O \to h$, whereas multi-step PTs only occur in a limited region roughly bounded by $0 \lesssim \lambda_{345} \lesssim 3$, $m_H \lesssim 250$ GeV and $m_A, m_{H^+} < 500$ GeV, which we scan with greater accuracy. In particular, we find that three-step PTs require $\lambda_{345} \lesssim 1.5$, while two-step PTs using a transient Hh phase are allowed only for $\lambda_{345} \lesssim 0.8$.

4.2 Direct detection

Before proceeding with the analysis of the resulting GW signal, we consider a further bound given by the direct detection experiments, which probe the spin-independent cross section of DM on nuclei. To this purpose, we show in fig. 3 the obtained spin-independent scattering cross section $\sigma_{\rm SI}$ as function of the

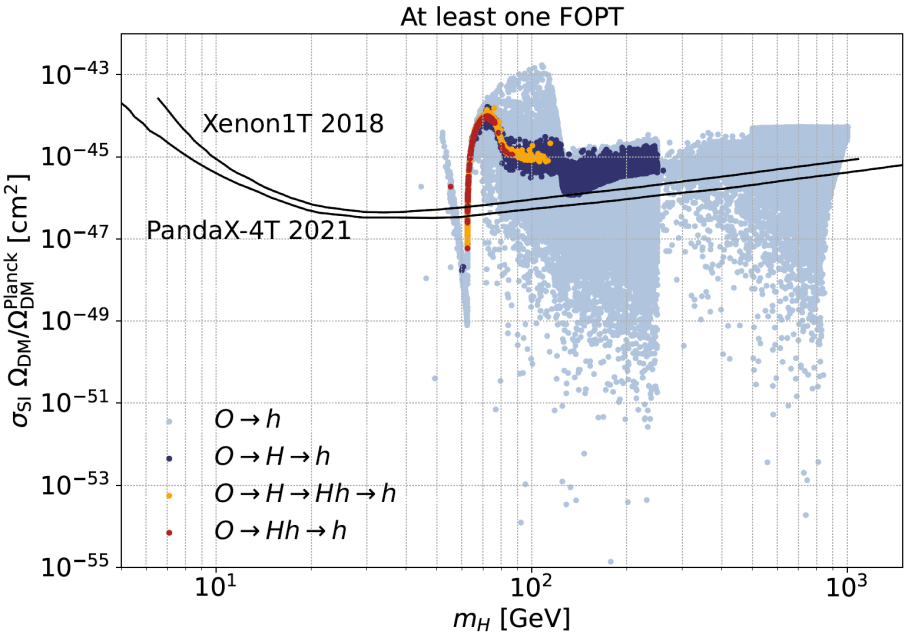

Figure 3: Spin-independent direct-detection cross section as function of the DM mass for transition patterns involving at least one FOPT. The colour code highlights the pattern type: one-step PT $O \to h$ (light blue), two-step PT $O \to H \to h$ (dark blue) and $O \to Hh \to h$ (red), as well as a three-step PT $O \to H \to Hh \to h$ (orange). The experimental bounds are taken from refs. [7, 35]. Points leading to DM overabundance are not shown.

DM mass, highlighting the different transition pattern identified. The analysis is presented for processes involving at least one FOPT. Because we allow for DM under-abundances, the plot has been obtained by re-scaling the cross section with the fraction $\Omega_{\rm DM}/\Omega_{\rm DM}^{\rm Planck}$, where $\Omega_{\rm DM}$ is the DM abundance produced by the IDM and $\Omega_{\rm DM}^{\rm Planck}$ the value given by the latest Planck measurement [3]. The indicated experimental bounds use the 2018 release of the XENON1T data [7] and the 2021 PandaX-4T result [35].

As we can see, most of the multi-step PTs fall above of the considered exclusion bounds. These processes may still occur near the Higgs resonance region ($m_H \simeq m_h/2$), where resonance effects allow for the lower values of the λ_{345} coupling required by these solutions. Another region of interest is for $m_H \in [120, 160]$ GeV, resulting in a signal borderline with the current exclusions for processes involving at least one FOPT. Contrary to the Higgs resonance region, these solutions select only multi-step PTs following the pattern $O \to H \to h$ and yield underabundant DM.

4.3 Gravitational wave

The GW signals supported by the IDM parameter space are shown in fig. 4, where we depict the value of the the peak of the power spectrum $h^2\Omega_{\rm GW}^{\rm peak}$ and the associated frequency at this peak $f^{\rm peak}$ for each point of scan performed.

The obtained GW signals are always dominated by the sound wave contribution. We also display the sensitivity curves of near future GW detectors LISA [40, 5], BBO [20, 21] and DECIGO [41, 29]. LISA, in particular, will probe mostly one-step transitions $O \to h$ and part of the solutions using the

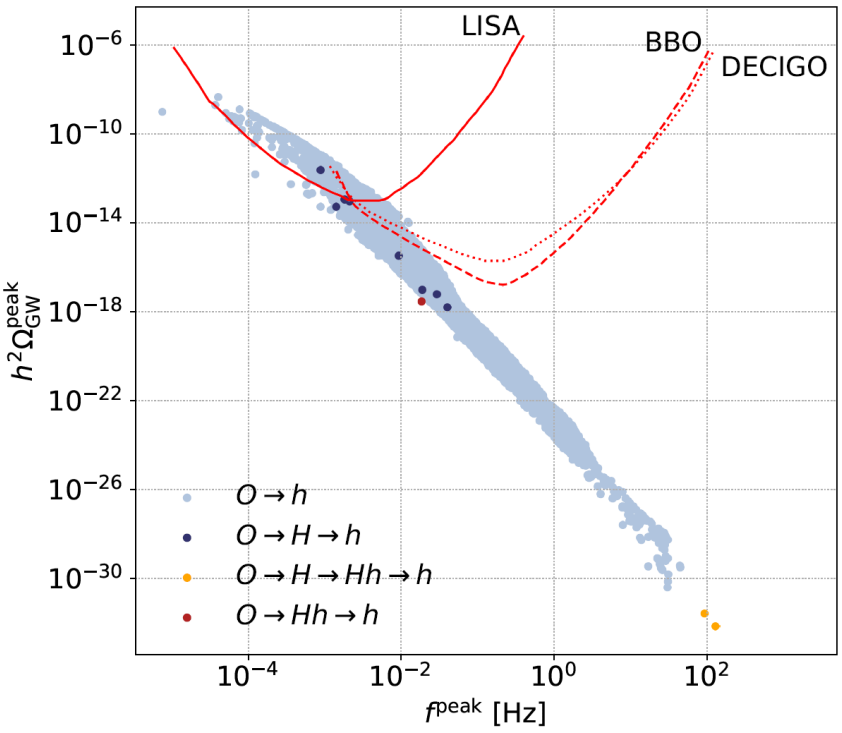

Figure 4: GW signal $h^2\Omega_{\rm GW}^{\rm peak}$ as a function of the frequency f for the considered parameter space. The colour code indicates the PT pattern. Points leading to DM overabundance and excluded by Xenon1T are not shown.

$O \to H \to h$ pattern. Overall, we see that single-step PTs tend to produce stronger signals. Finally, no points yielding a detectable GW signal by LISA, BBO or DECIGO, while satisfying Planck relic density constraint were found.

5 Conclusion

With the present paper we intended to address a thorough study of the cosmic phase transitions as well as the implied gravitational wave signals, with a comprehensive exploration of the phase structure and possible transitions supported by the inert doublet model. In our work we took into account available collider constraints, electroweak precision observables and theoretical bounds imposed by stability of the potential and perturbativity. Furthermore, the latest results of dark matter experiments have been used to investigate the properties of the neutral scalar component of the inert doublet, assumed to provide at least a subdominant dark matter component.

Our study of the thermal evolution of the scalar potential has given a full characterization of the possible phase transition patterns supported by the inert doublet model (see fig. 1). Although in most of the parameter space the electroweak vacuum is reached through a single phase transition, our analysis shows well-defined parameter regions where the electroweak vacuum is reached via a chain of consecutive phase transitions. Both two-step and three-step phase transitions with different transient phases (where only the inert doublet or both the doublets acquire a vacuum expectation value) are possible. Multi-step

transitions can occur when the inert doublet components are not heavier than a few hundred GeV and couplings have moderate values, as shown in fig. 2 for patterns involving at least one first-order step.

By cross-correlating the identified phase transition patterns with dark matter phenomenology, we find that the inert doublet model can explain the observed relic abundance only in a part of its parameter space where the electroweak vacuum is reached through single-step processes of either order. Although multi-step phase transition patterns are associated with a significant dark matter underdensity, we see that dark matter direct detection experiments are able to tightly constrain these solutions. Focusing on patterns that involve at least one first-order phase transition, fig. 3 shows that the direct detection bounds allow for multi-step phase transitions almost exclusively for dark matter masses close to half the Higgs boson mass.

Finally, after applying the results of direct detection searches as a further constraint, we have investigated the gravitational wave spectra produced by different phase transition patterns. The results, gathered in fig. 4, show that one-step processes dominate the signal. Future gravitational wave experiments will probe a part of these solutions yielding a significant dark matter underdensity, implying that the detection of a compatible signal would require another dark matter component. Whereas few points with multiple first-order phase transitions fall above the sensitivity curves of the considered experiments, we find that the generated gravitational signal is always strongly dominated by the transitions initiated during the transient phase at intermediate temperature. Therefore, it is highly unlikely that such transitions will induce a gravitational wave signal with two separate distinguishable peaks at different frequencies.

Acknowledgements

This work was supported by the Estonian Research Council grants PRG434 and PRG356, by the European Regional Development Fund and the programme Mobilitas Pluss grants MOBTT5 and MOBTT86, and by the EU through the European Regional Development Fund CoE program TK133 "The Dark Side of the Universe". The work of LDR has been partially supported by a fellowship from "la Caixa" Foundation (ID 100010434) and from the European Union's Horizon 2020 research and innovation programme under the Marie Sklodowska-Curie Action grant agreement No 847648.

References

1. ATLAS Collaboration, Constraining the Dark Sector with the monojet signature in the ATLAS experiment, in: ATL-PHYS-PUB-2021-020
2. G. Aad *et al*, Phys. Lett. B, 716:1-29 (2012).
3. N. Aghanim *et al*, Astron. Astrophys., 641:A6 (2020).
4. D. S. Akerib *et al*, Phys. Rev. Lett., 118(2):021303 (2017).
5. LISA Collaboration, Laser Interferometer Space Antenna, in: eprint arXiv:1702.00786
6. G. W. Anderson *et al*, Phys. Rev. D, 45:2685-2698 (1992).
7. E. Aprile *et al*, Phys. Rev. Lett., 121(11):111302 (2018).
8. A. Arhrib *et al*, Phys. Rev. D, 85:095021 (2012).

9. ATLAS collaboration, Combined measurements of Higgs boson production and decay using up to 139 fb^{-1} of proton-proton collision data at $\sqrt{s} = 13$ TeV collected with the ATLAS experiment, in: ATLAS-CONF-2021-053

10. R. Barbieri *et al*, Phys. Rev. D, 74:015007 (2006).

11. G. Belanger *et al*, Phys. Rev. D, 91:115011 (2015).

12. G. Belanger *et al*, Eur. Phys. J. C 81(3):239 (2021).

13. A. Belyaev *et al*, Phys. Rev. D, 97(3):035011 (2018).

14. J. Bernon *et al*, JHEP, 05:151 (2018).

15. Q. H. Cao *et al*, Phys. Rev. D, 76:095011 (2007).

16. S. Chatrchyan *et al*, Phys. Lett. B, 716:30-61 (2012).

17. J. M. Cline *et al*, JHEP, 11:089 (2011).

18. J. M. Cline *et al*, Phys. Rev. D, 55:3873-3881 (1997).

19. S. R. Coleman *et al*, Phys. Rev. D, 7:1888-1910 (1973).

20. V. Corbin *et al*, Class. Quant. Grav., 23:2435-2446 (2006).

21. J. Crowder *et al*, Phys. Rev. D, 72:083005 (2005).

22. C. Delaunay *et al*, JHEP, 04:029 (2008).

23. N. G. Deshpande *et al*, Phys. Rev. D, 18:2574 (1978).

24. L. Dolan *et al*, Phys. Rev. D, 9:3320-3341 (1974).

25. S. Fabian *et al*, JCAP, 09:011 (2021).

26. I. F. Ginzburg *et al*, Phys. Rev. D, 82:123533 (2010).

27. W. Grimus *et al*, Nucl. Phys. B, 801:81-96 (2008).

28. D. J. Gross *et al*, Rev. Mod. Phys., 53:43-80 (1981).

29. S. Kawamura *et al*, PTEP, 2021(5):05A105 (2021).

30. V. Khachatryan *et al*, JHEP, 02:135 (2017).

31. L. L. Honorez *et al*, JCAP, 02:028 (2007).

32. C. T. Lu *et al*, Phys. Rev. D, 106:035034 (2022).

33. E. Lundstrom *et al*, Phys. Rev. D, 79:035013 (2009).

34. E. Ma, Phys. Rev. D,73:077301 (2006).

35. Y. Meng *et al*, Phys. Rev. Lett., 127(26):261802 (2021).

36. R. R. Parwani *et al*, Phys. Rev. D, 45:4695-4705 (1992).

37. M. E. Peskin *et al*, Phys. Rev. Lett., 65:964-967 (1990).

38. M. E. Peskin *et al*, Phys. Rev. D, 46:381-409 (1992).

39. A. Pierce *et al*, JHEP, 08:026 (2007).

40. eLISA Collaboration *et al*, The Gravitational Universe, in: eprint arXiv:1305.5720

41. N. Seto *et al*, Phys. Rev. Lett., 87:221103 (2001).

42. C. L. Wainwright *et al*, Comput. Phys. Commun., 183:2006-2013 (2012).